A new pathway to correlate the octahedral tilt coupling and spin-orbit reconstruction at oxide interfaces

SUJIT DAS

sujitdas@iisc.ac.in

Indian Institute of Science, Bangalore   https://orcid.org/0000-0001-9823-0207

Jayjit Dey
Indian Institute of Science

Koushik Jagadish
Indian Institute of Science, Bangalore

Arka Bandyopadhyay
Indian Institute of Science

Sourav Chowdhury
Deutsches Elektronen-Synchrotron DESY

Moritz Hoesch
Deutsches Elektronen-Synchrotron DESY   https://orcid.org/0000-0002-0114-2110

Anju Ahlawat
UGC-DAE Consortium for Scientific Research

Feras Afaneh
The Hashemite University

Aryan Keshri
Indian Institute of Science

Basanta Roul
Indian Institute of Science

Saluru Krupanidhi
Indian Institute of Science

Mukul Gupta
UGC-DAE Consortium for Scientific Research

Ram Choudhary
UGC-DAE Consortium for Scientific Research

Thirumalai Venkatesan
National University of Singapore   https://orcid.org/0000-0001-9683-4584

Awadhesh Narayan

Indian Institute of Science

N. Ravishankar
Indian Institute of Science

Article

Keywords:

A new pathway to correlate the octahedral tilt coupling and spin-orbit reconstruction at oxide interfaces

Jayjit Kumar Dey[1]*, Koushik Jagadish[1]*, Arka Bandyopadhyay[2], Sourav Chowdhury[3], Moritz Hoesch[3], Anju Ahlawat[4,5], Feras Afaneh[6], Aryan Keshri[1], Basanta Roul[1,7], Saluru Baba Krupanidhi[1], Mukul Gupta,[4] Ram Janay Choudhary[4], Thirumalai Venkatesan[8#], Awadhesh Narayan[2], N. Ravishankar[1], Sujit Das[1#]

[1] Materials Research Centre, Indian Institute of Science, Bangalore- 560012, India

[2] Solid State and Structural Chemistry Unit, Indian Institute of Science, Bangalore- 560012, India

[3] Deutsches Elektronen-Synchrotron DESY, Notkestrasse 85, 22607 Hamburg, Germany

[4] UGC-DAE Consortium for Scientific Research, University Campus, Khandwa Road, Indore 452001, India

[5] Medicaps University, Rau, Indore 453331, India

[6] Department of Physics, Faculty of Science, The Hashemite University, P. O. Box 330127, Zarqa 13133, Jordan

[7] Central Research Laboratory, Bharat Electronics, Bangalore 560013, India

[8] Center for Quantum Research and Technology, University of Oklahoma, Norman, Oklahoma 73019, USA

*Authors contributed equally

[#]Corresponding authors e-mail address: (T.V) venky@ou.edu; (S.D) sujitdas@iisc.ac.in

Abstract

The direct experimental probing and detailed imaging of octahedral tilt, along with the control of magnetic ground state and spin-orbit occupancies in an artificially engineered heterointerface through the manipulation of strain via interface engineering, is the long-standing challenging issue addressed in this study. We introduce a novel methodology that involves the measurement of the projected O-O-O angles (OOO_{proj}) between the neighboring in-plane BO_6 octahedra of perovskite oxide (ABO_3), demonstrating a precise quantification of strain-manipulated octahedral tilt in atomically engineered $La_{0.7}Sr_{0.3}MnO_3$ (LSMO)/$LaCoO_3$ (LCO) bilayer interfaces. The pronounced octahedral tilt on $SrTiO_3$ (STO) substrate (under tensile strain) compared to $LaAlO_3$ (LAO) substrate (under compressive strain) correlates with the enhanced (suppressed) magnetism under tensile (compressive) strain in bilayer configuration, especially within the framework of bond angle geometry and spin-charge-orbital reconstructions, contrasting with strain effects reported on individual single-phase films. Interfacial orbital reconstruction, Co/Mn antiferromagnetic coupling and their manipulation under strain are quantified through X-ray linear dichroism (XLD) and X-ray magnetic circular dichroism (XMCD) measurements, further confirmed by both molecular orbital theory and Goodenough-Kanamori-Anderson rules. First principles calculations unveil a higher (lower) magnetic moment of individual magnetic atoms with tensile (compressive) strain, while also explaining the unusual interfacial antiferromagnetism arising from the interplay of out-of-plane and in-plane d-orbital occupations, and the role of bond angle geometry. This endeavor paves a potential method to manipulate the octahedral tilt and resultant perturbed crystal field energy to explore and tailor emergent phenomena at heterointerfaces via atomically precise strain-interface engineering.

The possibility for groundbreaking research lies at the interface of robust perovskite systems, where control of spin, charge, orbital, and lattice interactions holds immense possibilities from both fundamental and device perspectives.[1,2,3] To unravel the correlations among these diverse degrees of freedom, numerous approaches are being studied, including engineering of strain[4,5], interface[6], defects[7,8] and symmetry.[9,10] However, scant attention has been paid to the engineering of bonding geometry within and in-between metal–oxygen octahedra.[11] Particularly challenging is the precise quantification and systematic manipulation of oxygen octahedra tilting, rotation, shape alteration, as determining the positions of oxygen ions at interfaces through diffraction techniques or conventional electron microscopy, with unit-cell-by-unit-cell observation of the oxygen network, is exceedingly complex. Several models have been proposed to generally describe how oxygen octahedra tilting evolves at perovskite oxide interfaces with different patterns[12,13] and also presented octahedra tilting in antiperovskite oxide and halide perovskite via first-principles calculations.[14,15] However, these models often overlook differences in the direction of tilting axes, magnitude of tilting angles, and orientation of the interfaces among different tilted components which offer a novel and efficient method for tailoring a myriad of functional properties in transition metal oxides. Manipulation of octahedra tilting is a key parameter for controlling functional properties of oxides. In recent years, induced octahedral tilting ordering has demonstrated the potential for significant functional enhancements, such as magnetoelectric switching in multiferroics[16,17] and improved optoelectronic properties in inorganic halide perovskites.[18] Several approaches, such as epitaxial strain, thickness manipulation, Jahn-Teller distortion, and stoichiometry control/ cation off-centering, have also been suggested for tuning octahedral tilt and distortions.[19,20,21] Octahedral tilting can alter the point symmetry of B-site ions, thus influencing Jahn–Teller distortions linked to crystal-field splitting of d orbitals,[22] or breaking inversion symmetry,[23] which directly impact the hybridized states between oxygen p and neighboring A-site or B-sites orbitals, profoundly affecting the electrical, magnetic, and superconducting properties of numerous perovskite compounds.[24] However, their effectiveness is constrained by the demand for high-quality interfaces. Interestingly, the unstrained perovskite $LaCoO_3$ (LCO) is merely an insulator and non-magnetic (paramagnetic) material that exhibits a systematic temperature-dependent spin-state transition starting from a low spin state (LS, t_{2g}^6, S = 0) to an intermediate spin state (IS, $t_{2g}^5 e_g^1$, S = 1) or a high spin state (HS, $t_{2g}^4 e_g^2$, S = 2).[25,26,27] Nevertheless, the single layer LCO thin films can exhibit unusual ferromagnetic insulator (FMI) behavior with Curie

temperature (T_C) ranging from 24-92 K, depending on the substrate-induced strain.[15,16,17] The rare presence of FMI nature holds promise for applications in spin-filter magnetic tunneling and multiferroic-based spintronics device applications. In parallel, the interface of an insulating ferromagnetic LCO with a double-exchange half-metallic ferromagnetic manganite $La_{0.7}Sr_{0.3}MnO_3$ (LSMO) has aroused great interest due to its display of interfacial octahedra tilt, room temperature charge transfer, spin transition as well as orbital polarization.[28] Furthermore, the mixed-valency, as well as the half-filled e_g orbital of Mn^{3+} in LSMO, ensures the crucial role of its magnetic and electronic properties via lattice distortion and orbital ordering through strain engineering.[29,30,31] The microscopic origin of these observed effects, artful manipulation of magnetic ground states, spin-orbital reconstruction and their low temperature scenario in the presence of tensile strain and compressive strain (for instance using Aberration-Corrected Scanning Transmission Electron Microscopy (AC-STEM)), remain largely uncharted.

Furthermore, the octahedral tilt (even at room temperature) when subjected to tensile and compressive strains, provides a crucial pathway to explore multifunctional properties. This study aims to fill that gap by presenting experimental evidence of octahedral tilt and manipulation under tensile to compressive strain, showcased through AC-STEM. Herein this study, we employ a novel methodology incorporating O-O-O angles rather conventional B-O-B angles to precisely quantify and characterize the octahedra tilt by incorporating AC-STEM with a greater applicability across various perovskite (oxide, halide, antiperovskite) materials and exploring the impact of substrate-induced strain spanning from compressive to tensile. Our systematic study on X-ray absorption spectroscopy (XAS) clearly confirms the charge state, showcasing the genuine presence of high spin Co^{2+} and Mn^{4+} at the bilayer interfaces. X-ray linear dichroism (XLD) analysis suggests that strain controls the in-plane and out-of-plane orbital polarization switching at the heterointerfaces. X-ray magnetic circular dichroism (XMCD) depicts element-specific insights into the manipulation of interfacial magnetic ground state, correlating with the antiferromagnetic nature at Co/Mn interfaces and magnetometry data. Finally, first-principles calculations lend further support for the role of the octahedral tilt under strain and the reconstruction of spin-charge-orbital-lattice degrees of freedom. The obtained results highlight an attractive strategy to design, engineer, and manipulate the strain-interface controlled octahedra tilt and the resultant surface-to-interfacial tunable properties open up avenues for next-generation spintronic devices involving oxides.

Results and Discussions

Structural-Interfacial resolution and octahedra tilting. 5nm LSMO/10nm LCO bilayers (BL) films (with alternative growth sequence denoted as BL1 and BL2; where capped LSMO (top) on LCO film is denoted as BL1, while capped LCO (top) on LSMO film denoted as BL2), were grown on single crystalline (001)-oriented LaAlO$_3$ (LAO), SrTiO$_3$ (STO), and Pb(Mg$_{1/3}$Nb$_{2/3}$)O$_3$-PbTiO$_3$ (PMN-PT) substrates using a pulsed laser deposition system (details in Methods and Supplementary Fig.1a). Bragg reflections reveal the single crystalline phase of LSMO and LCO in the BLs, as well as gradual shifts of (00l) peaks towards lower angles from LAO to PMN-PT (Supplementary Fig.1b), indicating that the BLs on LAO are under compressive strain, while the BLs on STO and PMN-PT are under tensile strain. Simultaneously, the calculated out of plane lattice parameter for LSMO and LCO layers undergo an evolution from 3.94 to 3.89 Å and 3.84 to 3.80 Å respectively, while transitioning from LAO to PMN-PT substrates (Supplementary Fig.1c). The deposited BLs exhibited smooth surface, with an average root-mean-squared roughness value close to 300 pm for all the BLs as confirmed from atomic force microscopy (AFM) (Supplementary Fig.1d). In addition, x-ray reciprocal space mapping (RSM) along (103)-reflection confirms coherent strain of bilayers on LAO and STO i.e. the bilayers share the same in-plane lattice constant with LAO and STO (Supplementary Fig.1e-f), while bilayer on PMN-PT showed a vertical shift due to lattice relaxation, affirming compressive strain of BLs on LAO (LSMO: -2.07%, LCO: -0.5%), tensile strain on STO (LSMO: +0.9%, LCO: +2.4%), and higher tensile strain on PMN-PT (LSMO: +1.8%, LCO: +3.2%) (Supplementary Fig.1g).

The high-angle annular dark-field (HAADF) micrograph exhibits an atomically sharp interface between the film layers and the substrate of the BL on STO (Fig. 1a; details in Methods and Supplementary Fig.2), while high-resolution energy dispersive X-ray spectroscopy (EDS) was utilized to precisely locate multiple interfaces due to the insufficient contrast between LSMO and LCO layers (Fig. 1b-c). A similar investigation using HAADF-STEM and atomic-resolution EDS mapping was conducted on BL on the LAO substrate (Fig. 1d-f), revealing the distribution of Sr, Ti, Al, La, Mn, and Co atoms at atomically smooth interfaces. Notably, the Mn map was utilized to determine the precise number of LSMO layers, revealing that both samples consisted of 15 Mn layers. This information plays a key role in quantifying octahedral tilts across the interfaces, as discussed later. Additionally, STEM analysis of BLs on PMN-PT substrate indicated severe distortion in LSMO planes near the LSMO/PMN-PT interface (Supplementary Fig. 3a-c). This distortion manifested as the stretching of the in-plane lattice of the LSMO layer to fit into the larger

PMN-PT lattice, resulting in a local structural deformation and contrast variation. A form of edge dislocation, marked by a dashed circle (Supplementary Fig. 3d), accommodated the strain relaxation, with LSMO layers above the dislocation displayed uniform contrast and additional lattice planes compared to those below, indicating relaxation. These findings support observations from reciprocal space mapping (RSM), confirming relaxation in BLs on the PMN-PT substrate.

Octahedral tilts, a dominant factor in the physical behavior of perovskite oxides, were confirmed and quantified using the projected O-O-O angle (OOO_{proj}) between two in-plane neighboring octahedra. Since the presence of geometric tilt of the octahedra will inevitably cause a systematic displacement of the O atoms, a non-coplanarity in the in-plane O column positions is expected (which appears as a non-collinearity in the [110] projection under consideration). The OOO_{proj} angle will be 180° for perfectly coplanar O atoms, and any deviations from this indicate that the O atoms are non-coplanar. The OOO_{proj} angle can thus be used as a probe to primarily assess the presence of actual geometric octahedral tilt, while effectively filtering out other contributions such as the B-ion displacement and octahedral distortions. This method is also observed to be robust against experimental errors as compared to the conventional B-O-B angles (details in Supplementary Note IV). Furthermore, we have assumed that the projected B-O-B and O-O-O angles should ideally be the same, provided the B site ion is not displaced and the octahedra are stiff, as a first approximation to filter out the other components (details in the methods section and Supplementary Fig. 4-6). This is shown schematically (Fig. 2a-c) for a hypothetical perovskite with a displaced B-ion, a standard STO lattice without any distortion/tilting, and LSMO with actual octahedra tilt, respectively (details in Methods). Simultaneous HAADF and annular bright field (ABF) imaging of the BL on STO facilitates the direct localization of cations and oxygen atoms, which is crucial for comprehending the octahedral tilt behavior (Fig. 2d-e; details in Methods). The absence of octahedral tilt in the STO substrate region is evident, with an OOO_{proj} angle close to 180°, signifying coplanar oxygen atoms in any given BO plane (Fig. 2f-g). However, a drastic change occurs across the LSMO/STO interface, with the OOO_{proj} angle reaching ~173° up to 5 uc, indicating non-coplanar oxygen atoms due to octahedral tilt in the LSMO layer. The OOO_{proj} angle variation continues throughout the LSMO layer, reaching ~175° at the LCO/LSMO interface. Digitally magnified micrographs of the LCO/LSMO and LSMO/STO interfaces (Fig. 2h-i) reveal a clear signature of octahedral geometry, with observable alternating shifts of oxygen atom positions both upward and downward along the horizontal Co−O−Co and Mn−O−Mn sequences.

This alternating shift suggests octahedral tilts in both CoO_6 and MnO_6 near the LCO/LSMO interface, providing valuable insights into the detailed structure of these perovskite oxide bilayers. In contrast, HAADF-ABF imaging of LCO/LSMO BL on LAO substrate (Fig. 2j-m) revealed a consistent tilt angle of ~178° across the LSMO and LAO layers, with a slight deviation to ~173° at the LCO/LSMO interface (Fig. 2m). Unlike the pronounced octahedral tilt observed in LSMO/LCO BL on STO, the LSMO/LAO and LSMO/LCO interface displayed a constant tilt angle (Fig. 2n-o). The possibility of the octahedral tilt into the plane of the figure (along an axis in the plane of the figure), was considered as a possible explanation for the non-appearance of the octahedral rotation in the experimental image, which is possible due to the absence of 4-fold symmetry in LSMO and LCO layers (details in Method, Supplementary Fig. 7). Further investigation using foils sectioned along a perpendicular orientation showed exactly the same behavior, ruling out the possibility that the absence of rotation was an experimental artifact (Supplementary Fig. 2, 7-9). The strain effect on the LSMO layer was evident in ABF imaging, corroborated by peak pair analysis (PPA) strain mapping (Supplementary Fig. 10). BL on STO exhibited different strain which is consistent with XRD and RSM (Q_z) results. This substantiates the fact that compressive strain at the LSMO/LAO interface suppresses octahedral tilt in the LSMO layer of the BL films.

Tuning orbital occupancy: linear dichroism. To probe the impact of structural distortions on the charge reconstruction and orbital occupation in the BLs under strain, we performed element specific XAS and XLD measurements in total electron yield (TEY) mode (Figure 3, Supplementary Fig. 11; details in Methods). The features at the O K-edge XAS (Fig. 3a) show overlapped peaks within 526-533 eV due to O $2p$-Co $3d$ and O $2p$-Mn $3d$ hybridized region corresponding to excitations from the O $1s$ state. A clear distinction can be observed in this first feature between BLs, for BL1, both O $2p$-Co $3d$ and O $2p$-Mn $3d$ hybridized region are probed, however, for BL2, only O $2p$-Co $3d$ hybridized region is revealed irrespective of strain. Another feature within the 536-538 eV range suggests the O $2p$-La $3d$/Sr $3d$ hybridized state, while higher energy features are attributed to the O $2p$-Co $4sp$/$4s$ and O $2p$-Mn $4sp$/$4s$ hybridized regions.[32,33,34] Mn $L_{3,2}$-edge XAS (Fig. 3b) show mixed-valence $Mn^{3+/4+}$ consistent with stoichiometric single layer LSMO films[35] and with more prominence of Mn^{4+} state in BL1 (Supplementary Note I). Concurrently, XAS of the Co $L_{3,2}$-edge (Fig. 3c) confirms our stoichiometric films with a mixed charge state of $Co^{2+/3+}$ ions where Co^{2+} is more prominent in BL1 compared to BL2. Notably, the

effective charge reconstruction i.e. charge transfer from Mn to Co, results in high spin Co^{2+} and Mn^{4+} states at the interface of BL1, which are intricately linked to crystal field splitting energy (Δ_{cf}), responsive to the variations of Co—O or Mn-O bond length and Co-O-Co or Mn-O-Mn bonding angle changes in determining the essential magnetic properties in BLs.

Furthermore, utilizing XLD, we further characterized the electronic properties of the BLs by probing the unoccupied d orbital states of the **Mn and Co** in the BLs. XLD is calculated by varying the incidence angle (α) of a linearly polarized x-ray beam with respect to the sample's surface plane (Fig. 3d-f and Supplementary Fig. 11; details in Method and Supplementary Note II). When $\alpha = 90°$ (dashed lines), i.e., the polarization of the x-ray is parallel to the in-plane direction of the sample surface ($I_{ab} = I_{ip}$ (E_{ip}//[100])), the XAS reflects the in-plane orbital occupancy of d_{xy} & $d_{x^2-y^2}$ orbital. When $\alpha = 30°$ (solid lines) i.e. the polarization of the x-ray is perpendicular to the sample surface, and the XAS probes the unoccupied states in both $d_{x^2-y^2}$ (and/or d_{xy}) and $d_{3z^2-r^2}$ (and/or d_{yz} and d_{zx}) orbitals, with $I_c = I_{oop} = [I_{90°}-I_{30°}\bullet sin^2 30°)/cos^2 30°]$ (E_{oop}//[001]). [36] To simplify the calculations, the signal of ($I_{ip}-I_{oop}$) can indirectly reflect the orbital asymmetry of the 3d band and is roughly proportional to the exact XLD signals (Fig. 3e, g). Negative to positive XLD values at both the Mn and Co $L_{3,2}$-edges of the BLs for tensile (BL on STO and BL on PMN-PT) to compressively strained (BL on LAO) suggest a highly occupied $d_{x^2-y^2}$ (and/or d_{xy}) orbital to highly occupied $d_{3z^2-r^2}$ (and/or d_{yz} and d_{zx}) orbital, respectively (Fig. 3e, g; Supplementary Fig. 11 and Supplementary Note II). Here, the orbital reconstruction is attributed to the strong covalent bond formed between the Mn-3d & Co-3d orbitals through the O-2p orbital across the interface and under different strains of the BLs induced by the substrates, elucidated in terms of molecular orbital theory (Supplementary Fig. 16-17 and Supplementary Note II).

Switching of ferromagnetic order and magnetic ground state. We now delve into a detailed understanding of macroscopic and microscopic insights into magnetic properties under compressive to tensile strain of the BLs (Fig. 4 and details in Methods). Thermal magnetization (M-T) of the BLs reveals finite magnetic moments, transitioning from ferromagnetic to paramagnetic near or above room temperature (Fig. 4a, c). In contrast to the previously reported single-layer 10 nm LSMO ($T_C = 260$ K) and LCO ($T_C = 80$ K),[37] the BL on STO shows distinctive transitions: a paramagnetic-to-ferromagnetic shift (attributed to LSMO, T_C ~320 K), followed by a second transition at 77 K (attributed to LCO). Here, the tensile strain alone proves insufficient for stabilizing LCO's long-range ferromagnetic order of the BL on STO.[38] Additionally, the

suppression of CoO_6 octahedral rotations needs to be considered for the modification of e_g orbital ordering configuration, leading to a spin-state transition to a ferromagnetic state.[39] Through our AC-STEM data (Fig. 2g), we observe the suppression of CoO_6 octahedral rotations, as measured using the OOO_{proj} angle, thereby manipulating Co orbital occupancy, Co-O bond length and Co-O-Co bond angle, ultimately weakening crystal-field splitting and promoting an ordered high-spin state of Co ions.[40] Moreover, in BL1, a decrease of magnetization is observed around 184 K to 82 K, which is assigned to the pinned antiferromagnetic layers at the LSMO/LCO interfaces.[18] Notably, the tensile strain affect the octahedral rotation of the BLs (both on STO and PMN-PT substrates), resulting in an elevated value of T_C (LSMO) in comparison to the measurement recorded in the single-layer LSMO system (T_C = 260 K).[18] The results vividly illustrate the prevailing ferromagnetic nature of LCO and LSMO for both the BL1 and BL2. In contrast, for BL1 on LAO substrate, the magnetic moment exhibits a tendency towards antiferromagnetism. In this context, it has been recently demonstrated that LCO exhibits antiferromagnetism only when Co–O–Co bond angles are greater than approximately 163º.[41] Our microscopic AC-STEM study (Fig. 2m) strongly supports the origin of antiferromagnetism and suppressed ferromagnetism on LAO substrate due to geometrically modified LCO that exhibits equivalent Co–O-Co bond angles down to 172º, as measured using the equivalent OOO_{proj}. While in BL2 on LAO, a remarkable spin reorientation phenomenon is realized due to a competition between spins of antiferromagnetic LCO and ferromagnetic LSMO. Thus, the emerging antiferromagnetism in BL on LAO, resulting from engineered bond angle geometry, justifies the overall lower magnetization in relation to BL on other substrates. This indicates that not only the compressive strain imposed by LAO substrate but also the interfacial bond engineering effect caused by LSMO/LCO layer modifies the overall magnetic contributions. In the case of the BL on PMN-PT substrate, an enhancement in magnetization is observed around 310 K, attributable to the T_C of LSMO, and a pronounced jump occurs near 87 K due to the T_C of LCO. Compared to STO, PMN-PT exhibits a larger tensile strain, although T_C and magnetization are lower than STO, which can be correlated to the relaxation and the presence of edge dislocations in the LSMO layer, as seen from HAADF-STEM (Supplementary Fig. 3). Additionally, a genuine response of electric field dependent (typical electric field, E = 400V = 8 kV/cm^2) enhanced magnetization is recorded on BL2/PMN-PT (Supplementary Fig. 12). The field-dependent magnetization, M (H), for the bilayers, obtained at

10 K (Fig. 4b, d, detailed in Methods), reveals an intriguing trend and correlates with the higher (lower) magnetization for tensile (compressive) strain.

To gain a proper understanding of the magnetic properties, especially the interfacial magnetization, elemental specific XMCD measurements are performed on the BLs at both the Mn and Co $L_{3,2}$-edge at 50K and room temperature (Fig. 4e-f and Supplementary Figs. 13-15). In the BL1, it is crucial to highlight that the XMCD signals exhibit opposite signs at the Co and Mn L-edges at 50K, providing evidence for the antiparallel alignment of interfacial Mn/Co moments for the BL on STO and BL on PMN-PT, which is consistent with the macroscopic magnetic observation. Interestingly, for BL on LAO, the near absence of Co XMCD signal reveals that LCO has drastically suppressed magnetism of the BL on LAO. This antiparallel Mn/Co moment orientation can be further elucidated through molecular orbital considerations (Supplementary Fig. 16-19, Supplementary Note III). For the BL under compressive strain (BL on LAO), the majority Mn $d_{3z^2-r^2}$ electron occupies a bonding orbital with the corresponding Co orbital, aligning parallel to the majority t_{2g} spins of Mn in accordance with Hund's rule (Supplement Figs. 16). Conversely, the minority Co t_{2g} d_{yz} and d_{zx} electrons occupy bonding orbitals alongside the corresponding Mn orbitals, exhibiting an antiparallel alignment with the localized Mn t_{2g} spins, thereby inducing an antiferromagnetic Mn/Co ordering at the interface of the BL (Supplementary Fig. 16). It is noteworthy that both LSMO and LCO under strained conditions exhibit a ferromagnetic state. Analogously, in the case of BL under tensile strain (BL on STO and BL on PMN-PT), an interfacial antiparallel Mn/Co alignment is also established (Supplementary Fig. 17). This unusual interfacial antiferromagnetic Mn/Co ordering in lieu of vivid ferromagnetism of the BLs are further confirmed through Goodenough-Kanamori-Anderson (GKA) rules[33,34]. According to the GKA rules, the Mn $d_{3z^2-r^2}$ -(O $2p_{zz}$)-Co d_{yz} and Mn $d_{3z^2-r^2}$ -(O $2p_{zz}$)-Co d_{zx} interactions in the BLs are antiferromagnetic in nature (Supplementary Figs. 18-19) similar to LSMO/BaTiO$_3$[42] heterostructures. Furthermore, the non-zero Mn L-edge XMCD at room temperature (300 K) confirms the ferromagnetic ground state of the LSMO layer in the BLs on STO and PMN-PT (BL under tensile strain). However, there is no such magnetic order observed for the BL on LAO, which is further confirmed by macroscopic magnetization data (Fig. 4 and Supplementary Fig. 14). Thus, strain-interface engineering plays a key role in manipulating magnetic properties in Co/Mn heterostructures.

Theoretical results. Furthermore, to establish the theoretical foundation of our experimental results, we have carried out first-principles calculations on LSMO-LCO BLs (Fig. 5a). At first, the self-consistent ground state geometry of the BLs has been achieved under unstrained conditions with the antiferromagnetic coupling between the ferromagnetic LSMO and LCO layers, consistent with our experimental observations. Under unstrained conditions, the average magnetic moment of Mn and Co atoms is obtained as $3.17\mu_B$ and $1.99\mu_B$, respectively. Furthermore, the choice of strain value, ± 2 % strength in both tensile and compressive strain, is adequate as it essentially helps to explore the underlying physics through a sizable strain-driven magnetic response. In the case of tensile strain, the average magnetic moments of the individual Mn and Co atoms are increased to the value 3.19 μ_B and $2.07\mu_B$, respectively in the BLs. On the contrary, the average magnetic moment of Mn and Co under compressive strain is significantly decreased to $3.13\mu_B$ and $1.70\mu_B$, respectively (Fig. 5b). Therefore, it is qualitatively evident that the application of strain, particularly the compressive one, exhibits an appreciable influence on the magnetic moment of the Co atom. This strain-driven magnetic moment change can be explained more accurately by the asymmetric projected density of states (PDOS) for spin-up and spin-down electrons, especially the d-orbitals of Mn and Co atoms, as depicted in Fig. 5c-e, where contributions of the other d-orbitals are also explored (Supplementary Fig. 20-21). To understand the role of strain on different in-plane and out-of-plane d-orbital, we reveal the proportion by which the in plane ($d_{x^2-y^2}$) and out-of-plane ($d_{3z^2-r^2}$) occupied d-orbitals of the magnetic atoms (say, Mn) change with application of external strain. We note that the proportion of the occupied in-plane d-orbitals invariably increases (decreases) by ~3% with the application of tensile (compressive) strain. On the contrary, the out-of-plane d-orbitals become more (less) occupied in the case of compressive (tensile) strain. It is worth mentioning that the other in-plane d_{xy} orbital also exhibits similar behavior as $d_{x^2-y^2}$. These first principles result on the orbital occupancy lend support to our experimental observations on XAS and XLD measurements (Fig. 3). This change in magnetic moment of Mn and Co atom with external strain can be well-understood from the modified B-O-B angle. In particular, the Mn-O and Co-O bond length (Supplementary Table1) as well as the Mn-O-Mn and Co-O-Co angle of the LSMO and LCO layers in the BLs invariably decrease (increase) and move far away from (closer to) $180°$ with increasing strength of tensile (compressive) strain. Moreover, we want to focus particularly on the Mn-O-Co angle at the interface $\boldsymbol{\alpha_1}$ along two crystallographic directions (**b**, **c**) and (**-b**, **c**), denoted as $\boldsymbol{\alpha_1}$ and $\boldsymbol{\alpha_2}$. These angles $\boldsymbol{\alpha_1}$ and $\boldsymbol{\alpha_2}$ decrease (in tensile strain) by

$0.56°$ and $0.96°$, respectively while increase by $2.56°$ and $1.30°$, respectively for compressive strain. We note that the OOO_{Proj} angle acts as an alternative to the corresponding B-O-B angle for LSMO/LCO interface, which changes more (less) with compressive (tensile) strain, and its variation is pronounced in the case of compressive strain, as also evident from the experimental observation (Fig. 2). Consequently, the crystal field splitting for MnO_6 octahedra near the interface experiences 1.04 times increase with compressive strain (-2%) and decreases by 0.99 times with tensile (2%) strain while for CoO_6 octahedra, increases by 1.05-fold with compressive (-2%) strain and decreases by 0.78-fold with tensile (2%) strain. We note that these octahedra tilting significantly determines the orbital occupancy of the *d*-orbital, consequently influencing the magnetic properties of the LSMO/LCO bilayer interfaces.

Conclusion. In conclusion, our new methodology has unveiled a novel strategy that utilizes OOO_{proj} angles, replacing the traditional BOB_{proj} angles, to efficiently explore oxygen octahedral tilt in perovskite oxides. Here, we disclose the effects of substrate-induced epitaxial strain on switching the spin state and orbital occupancy between in-plane and out-of-plane orbitals through synchrotron based XAS-XMCD techniques. The manipulation of octahedral tilt offers a conceptually novel revelation for the longstanding issue of the antiferromagnetic nature of cobaltate/ manganite interface overcoming its ferromagnetic nature. More importantly, we reveal a previously unreported octahedra tilt that directly correlates with the enhanced magnetism of LCO layers in BL on STO, while strain-mediated OOO_{proj} angle variation depicts the real absence of ferromagnetism of LCO in the BL on LAO substrate. XMCD results and the explanation in the light of molecular orbital theory confirm the antiferromagnetic involvement of Mn/Co interfaces. First principles theoretical calculations further clearly demonstrate the scenario of strain induced Co/Mn individual magnetic moment contribution and interfacial antiferromagnetism, in-plane and out-of-plane orbital occupation, and detailed bond angle geometry specifically in terms of OOO_{proj}. Thus, the interplay of octahedral tilt and charge-spin-orbital reconstruction in oxide heterostructures offers a promising strategy to interface-engineer physical properties, such as voltage-controlled strain or orbital filling. This approach holds significant promise for the development of novel next generation low energy spintronics, including magnetic tunnel junction, magnetic field sensing, and devices for magnetic storage applications.

METHODS

Sample preparation. The [LaCoO$_3$ (LCO)/La$_{0.7}$Sr$_{0.3}$MnO$_3$ (LSMO)] BLs were synthesized on single-crystalline LAO (001), STO (001), PMN-PT (001) substrates via reflection high energy electron diffraction (RHEED)-assisted pulsed laser deposition (KrF laser, λ = 248 nm). Here BLs are designed in two reverse sequences where capped LSMO (top) on LCO thin film is denoted as BL1, while capped LCO (top) on LSMO thin film is as BL2. Firstly, 5 nm LSMO was grown on all the substrates at substrate temperature (T$_S$) of 700 °C in 100 mTorr of oxygen pressure (P$_{O2}$). On this LSMO bottom layer, a 10 nm LCO top layer was grown with (P$_{O2}$) = 300 mTorr at the same T$_S$. A similar protocol was followed to grow the bilayer configuration consisting of a bottom layer of 10 nm LCO and top layer of 5 nm LSMO on those substrates at the same T$_S$ with P$_{O2}$ = 300 and 100 mTorr respectively. For all materials, the laser fluence was 0.6 J/cm^2 with a repetition rate of 4 Hz. After deposition, the bilayers were annealed for 30 min in 50 Torr of oxygen pressure to ensure the correct oxygen stoichiometry and then cooled down to room temperature at that oxygen pressure.

Structural and surface morphology characterization. X-ray diffraction (XRD), and reciprocal space mapping (RSM) measurements were carried out using a Bruker D8 discover diffractometer with Cu-$K\alpha$ radiation (λ = 1.54056 Å). The morphologies and roughness of substrates as well as samples were characterized with an Asylum Research Oxford 3D origin plus AFM in the tapping mode.

Magnetic measurements. Temperature and field dependence microscopic magnetic measurements are performed by using a Quantum Design VSM SQUID (superconducting quantum interference device). The temperature-dependent (*M-T*) in-plane ($\mu_0 H//100$) magnetic measurements were recorded at 0.1 T after the field cooling (FC) at 0.1 T. The magnetic hysteresis curves (M-H) are measured along in-plane ($\mu_0 H//100$) direction at 10K after the field cooling samples (FC) at 0.1 T. The magnetization of the films was acquired by subtracting the diamagnetic signals from the substrates and the plastic tube. The magnetization is expressed in Bohr magnetons per total number of pseudo-cubic unit cells.

STEM measurements. The cross-sectional samples for STEM were prepared using an FEI Scios FIB-SEM dual beam system using Ga$^+$ ions. The single-crystal foil was thinned along the particular zone axis required (i.e,. STO, LAO [110]), to minimize the tilting required in the STEM as too much tilting (roughly > 5°) will cause thickness related artifacts in the ABF mode. The final

cleaning was done using an Ar ion beam in a Gatan PIPS II system. The STEM imaging was performed in an FEI Titan Themis equipped with a CEOS probe C_s corrector, operated at 300 kV. A 70 μm C2 aperture and a camera length of 160 mm was used, such that the ABF image could be acquired using the DF2 detector, while simultaneously acquiring the HAADF image using the high angle detector. The sample was tilted to the zone axis and allowed to stabilize for at least 1 hour, before acquiring the data. Further, the scan dimension was reduced to allow a longer dwell time (8 μs) per pixel, to improve the signal-to-noise ratio, while minimizing drift. The energy dispersive X-ray spectroscopy (EDS) mapping was done using the Velox software, incorporating a beam current of ~150 pA. The strain concentration in the films were extracted from the HAADF micrographs using the Peak pair analysis (PPA) Digital Micrograph plug-in from HREM Research Inc.[43]

Octahedra tiling measurement approach. The coordinates of the A, B and O sites in the ABF micrographs were extracted from the Fourier filtered ABF micrograph by fitting gaussians to the peak positions using the Atomap package. The B and O coordinates were then used to measure the in-plane projected B-O-B, O-B-O and O-O-O angles between the multiple octahedra, calculated using a custom script written in Python. All the angles are measured between two consecutive oxygen sharing octahedra along a row (i.e., the BO plane), taking two octahedra at a time (Code details in Supplementary Note IV). To validate the script, ABF images of STO and LSMO were simulated using Dr. Probe software (Supplementary Fig. 4a and 4f). The simulated images were subject to the Atomap script to extract the coordinates of the B and O sites. The coordinates were then used in the custom script to find the B-O-B, O-B-O and O-O-O angles which were mapped to the respective coordinates and plotted as contours and row averaged scatter plots (with the standard deviation) for STO and LSMO (Supplementary Fig. 4c, d, e and 4h, i, j). Since we can assume (to a first approximation) that the B-O-B, O-B-O and O-O-O angles are all equal to 180° in the STO, we confirm that the Gaussian fitting through the Atomap script, and the custom angle calculator script succeeds sufficiently. However, when applied to an experimental ABF image of STO, it is observed that only the O-O-O angle is robust and gives the correct value as tabulated in Supplementary Fig. 5. The errors in the B-O-B and O-B-O angles might be the result of experimental error of B site positions or some distortions related to the B sites in the micrograph and will require further investigation (Supplementary Note IV). But since the B-O-B and O-O-O angles can be assumed to be equal in LSMO (Along the projection considered, and to a first

approximation, schematic in Supplementary Fig. 4g), either can be used to quantify the octahedral tilting. Thus, the O-O-O angle is used throughout the current article. Finally, the tilt mapping procedure has been applied to an experimental LSMO/STO interface micrograph. The coplanarity of the O sites in the STO layer and the non-coplanarity of the O sites in the LSMO layers is clearly observed (Supplementary Fig. 6b-c). A checkerboard pattern is observed in the B-O-B angle contour map (Supplementary Fig. 6d), similar to the octahedra tilt pattern in LSMO, but the absolute tilt angle is deemed inaccurate as the substrate B-O-B angle comes out to be 160°. However, the O-O-O angle from the substrate is closer to 180°, and a clear deviation in the octahedral tilt (close to 10°) is observed when going from the substrate to the film (Supplementary Fig. 6f). The O-O-O angles are used throughout the article and more work is required for the complete understanding of the robustness.

XAS, XMCD and XLD measurements. Element sensitive XAS and XMCD measurements were performed at P04 beamline, PETRA III, DESY, Germany at the Mn and Co L- -edges and O K-edges in surface-sensitive total electron yield (TEY) modes both at 50 K and 300 K. The process was carried out under a background vacuum of 8×10^{-7} Torr. The normalization of spectra was performed so that the L_3 pre-edge spectral region was set to zero, in addition to the post L_2 edge region set to one. Circularly polarized x-rays with ~100% polarization was used in normal incidence with respect to the sample surface and parallel to the applied magnetic field. The XMCD was obtained by taking the difference of the XAS spectra of right circularly polarized light (μ^+) and left circularly polarized light (μ^-), i.e., $\mu^+ - \mu^-$, by flipping the magnetic field of ±0.6T at a fixed x-ray helicity. The intensity and the detailed line shape of the XAS spectra reveal information of different valence states, while those of the XMCD spectra indicate the corresponding magnetic ground states. XLD measurement was performed at BL01 beamline of Indus-2 synchrotron radiation source at RRCAT, Indore using linearly polarized x-rays with polarization vector (E) parallel to the in-plane or out-of-plane direction of the sample plane, respectively in the TEY mode at 300 K.

Theoretical calculations. The first-principles calculations for LSMO-LCO heterostructure are performed under the spin-polarized density functional theory (DFT) framework as implemented in the quantum espresso code. [44,45] We have employed the Perdew-Burke-Ernzerhof (PBE) form for the exchange-correlation functional[46] for all the calculations related to the unstrained and strained cases. Furthermore, the kinetic energy cut-off is set as 75 Ry in our study using the

ultrasoft pseudopotentials[47] to describe the core electrons. The Brillouin zone was sampled over a uniform Γ-centered k-mesh of $10 \times 10 \times 1$. A vacuum of 15 Å is considered along the crystallographic c-axis to avoid any spurious interaction between the periodic images. Finally, the correlation effects for the Mn and Co sites have been evaluated using the DFT+U method with the Hubbard U parameters 2 eV and 2.7 eV, respectively.

References

[1] Hwang, H. et al. Emergent phenomena at oxide interfaces. Nat. Mater. 11, 103–113 (2012).

[2] Tokura, Y. & Nagaosa, N. Orbital physics in transition-metal oxides. Science 288, 462–468 (2000).

[3] Bristowe, N. et al. Ferromagnetism induced by entangled charge and orbital orderings in ferroelectric titanate perovskites. Nat Commun 6, 6677 (2015).

[4] Pesquera, D. et al. Beyond Substrates: Strain Engineering of Ferroelectric Membranes. Adv.Mater. 32, 2003780 (2020).

[5] Torres, P. et al. Giant electrophononic response in $PbTiO_3$ by strain engineering. Phys. Rev. Lett. 123, 185901 (2019).

[6] Bang, J. et al. Interface engineering for substantial performance enhancement in epitaxial all-perovskite oxide capacitors. NPG Asia Mater 15, 4 (2023).

[7] Sun, Y. et al. Defect engineering in perovskite oxide thin films. Chem. Commun. 57, 8402-8420 (2021).

[8] Menéndez, C. et al. Oxygen-vacancy induced magnetic phase transitions in multiferroic thin films. npj Comput Mater 6, 76 (2020).

[9] Zhang, J. et al. Symmetry mismatch-driven perpendicular magnetic anisotropy for perovskite/brownmillerite heterostructures. Nat Commun 9, 1923 (2018).

[10] Ding, X. et al. Crystal Symmetry Engineering in Epitaxial Perovskite Superlattices. Adv. Funct. Mater. 31, 2106466 (2021).

[11] Jeong, S. G. et al. Propagation Control of Octahedral Tilt in $SrRuO_3$ via Artificial Heterostructuring. Adv. Sci. 7, 2001643 (2020).

[12] R. Beanland Structure of planar defects in tilted perovskites, Acta Crystallogr. A67 191–199 (2011).

[13] Liao, Z. et al. Long-range domain structure and symmetry engineering by interfacial oxygen octahedral coupling at heterostructure interface, Adv. Funct. Mater. 26 6627–6634 (2016).

[14] Garcia-Castro, A.C. et al. Octahedral distortion and electronic properties of the antiperovskite oxide Ba3SiO: First principles study, Journal of Physics and Chemistry of Solids 136 109126 (2020).

[15] Junwen, Y. et al. Tuning Octahedral Tilting by Doping to Prevent Detrimental Phase Transition and Extend Carrier Lifetime in Organometallic Perovskites, *Journal of the American Chemical Society 145* (9), 5393-5399 (2023)

[16] Zhao, H. J. et al. Magnetoelectric effects via pentalinear interactions Phys. Rev. B 92, 235133 (2015).

[17] Yang, Y. et al. Prediction of a Novel Magnetoelectric Switching Mechanism in Multiferroics Phys. Rev. Lett. 112, 057202 (2014).

[18] Bechtel, J.S. et al. Octahedral tilting instabilities in inorganic halide perovskites Phys. Rev. Mater. 2, 025401 (2018).

[19] Chowdhury, S. et al. Strain dependent spin-blockade effect realization in the charge-disproportionated $SrCoO_{2.5}$ thin films. Appl. Phys. Lett. 119 (2): 021901 (2021).

[20] J. W. Freeland et al Orbital control in strained ultra-thin $LaNiO_3$/$LaAlO_3$ superlattices. EPL 96 57004 (2011).

[21] Wakabayashi, Y.K. et al. Ferromagnetism above 1000 K in a highly cation-ordered double-perovskite insulator Sr_3OsO_6. Nat Commun 10, 535 (2019).

[22] Rondinelli, J. M. et al. Structure and Properties of Functional Oxide Thin Films: Insights From Electronic-Structure Calculations Adv. Mater. 23, 3363 (2011).

[23] Van Aken, B. B. et al. The origin of ferroelectricity in magnetoelectric $YMnO_3$ Nat. Mater. 3, 164 (2004).

[24] Cohen, R. E. Origin of ferroelectricity in perovskite oxides Nature 358, 136 (1992).

[25] Fujioka J. et al. Strain-sensitive spin-state ordering in thin films of perovskite $LaCoO_3$ Phys. Rev. B 92, 195115 (2015).

[26] Sterbinsky G.E. et al. Ferromagnetism and Charge Order from a Frozen Electron Configuration in Strained Epitaxial $LaCoO_3$ Phys. Rev. Lett. 120, 197201 (2018).

[27] Guo E-J. et al. Switchable orbital polarization and magnetization in strained $LaCoO_3$ films. Phys. Rev. Materials **3**, 014407 (2019).

[28] Li, X. et al. Impact of interfacial coupling of oxygen octahedra on ferromagnetic order in $La_{0.7}Sr_{0.3}MnO_3$/$SrTiO_3$ heterostructures. Sci Rep 7, 40068 (2017).

[29] Lepetit, M. et al. Interface effects in perovskite thin films. Phys. Rev. Lett. 108, 087202 (2012).

[30] Lee, J. S. et al. Hidden magnetic configuration in epitaxial $La_{1-x}Sr_xMnO_3$ films. Phys. Rev. Lett. 105, 257204 (2010).

[31] May, S. J. et al. Enhanced ordering temperatures in antiferromagnetic manganite superlattices. Nature Mater. 8, 892–897 (2009).

[32] Chowdhury, S. et al. Negative Charge-Transfer Energy in $SrCoO_{2.5}$ Thin Films: An Interplay between O-2p Hole Density, Charge-Transfer Energy, Charge Disproportionation, and Ferromagnetic Ordering. *ACS Appl. Electron. Mater.* 2, 12, 3859–3870 (2020)

[33] Jana, A. et al. Spectroscopic comprehension of Mott-Hubbard insulator to negative charge transfer metal transition in $LaNi_xV_{1-x}O_3$ thin films. Phys. Rev. B 106, 205123 (2022).

[34] Chowdhury, S. et al. Electronic Phase Switching in the Negative Charge Transfer Energy $SrCoO_x$ Thin Films with the Mottronic Relevancies. *ACS Appl. Electron. Mater.* 3, 7, 3060–3071 (2021).

[35] Trappen, R. et al. Electrostatic potential and valence modulation in $La_{0.7}Sr_{0.3}MnO_3$ thin films. Sci Rep 8, 14313 (2018).

[36] Tebano, A. et al. Evidence of orbital reconstruction at interfaces in ultrathin $La_{0.67}Sr_{0.33}MnO_3$ films. Phys. Rev. Lett. 100, 137401 (2008).

[37] Thota, S. et al. Structural and magnetic properties of ($La_{0.7}Sr_{0.3}MnO_3/LaCoO_3$) heterostructures. Appl. Phys. Lett. 113, 122405 (2018).

[38] Rondinelli, J. M. & Spaldin, N. A. Structural effects on the spin-state transition in epitaxially strained $LaCoO_3$ films. Phys. Rev. B 79, 054409 (2009).

[39] Li, D. et al. Emergent and robust ferromagnetic-insulating state in highly strained ferroelastic $LaCoO_3$ thin films. Nat Commun 14, 3638 (2023).

[40] Choi, W.S. et al. Strain-Induced Spin States in Atomically Ordered Cobaltites. *Nano Lett.* 12, 9, 4966–4970 (2012).

[41] Joshi, T. et al. Geometric influence on the net magnetic moment in $LaCoO_3$ thin films. Journal of Materials Research 38, 2274–2286 (2023).

[42] Wang, H. et al. Atomic-Scale Control of Magnetism at the Titanite-Manganite Interfaces. Nano Lett. 19, 3057– 3065 (2019).

[43] Galindo, Pedro L. et al. The Peak Pairs algorithm for strain mapping from HRTEM images. Ultramicroscopy 107, 1186–1193 (2007).

[44] Giannozzi, P. et al. Advanced capabilities for materials modelling with Quantum ESPRESSO. Journal of Physics: Condensed Matter 29, 465901 (2017).

[45] Giannozzi, P. et al. QUANTUM ESPRESSO: a modular and open-source software project for quantum simulations of materials. Journal of Physics: Condensed Matter 21, 395502 (19pp) (2009).

[46] Perdew, J. P. Generalized Gradient Approximation Made Simple. Physical review letters 77, 3865 (1996).

[47] Vanderbilt, D. Soft self-consistent pseudopotentials in a generalized eigenvalue formalism. Phys. Rev. B 41, 7892–7895 (1990).
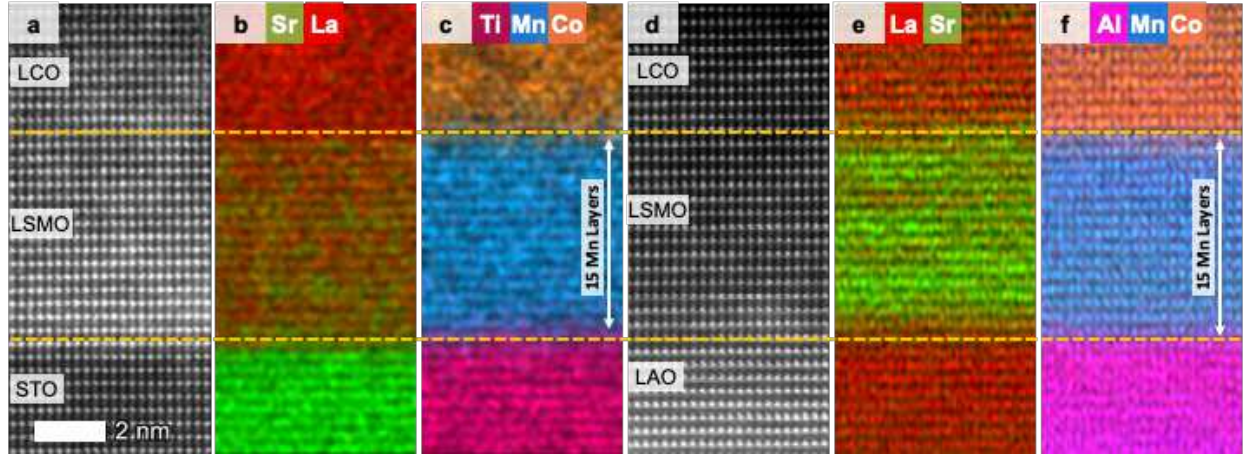
Figures

Figure 1| Microscopic structural characterization of the LSMO/LCO BLs under strain. a, Atomically resolved STEM-HAADF micrograph of the BL2 on STO substrate. **b-c**, EDS elemental maps from the same region as **(a)**, using which the interfaces are marked and observed to be atomically sharp, with a diffuseness of the order of one unit cell. **d-f,** Atomically resolved STEM-HAADF micrograph of the BL2 on LAO substrate and the corresponding EDS maps. The Mn map can be used to pinpoint the two interfaces, using which it is observed that the LSMO film consists of 15 Mn layers as shown in **(c)** and **(f)**; This information can be correlated with the ABF micrograph to exactly measure the variation in the octahedral tilts across the interfaces, down to the unit cell level. The scale is the same as shown in **(a)** for all the images.
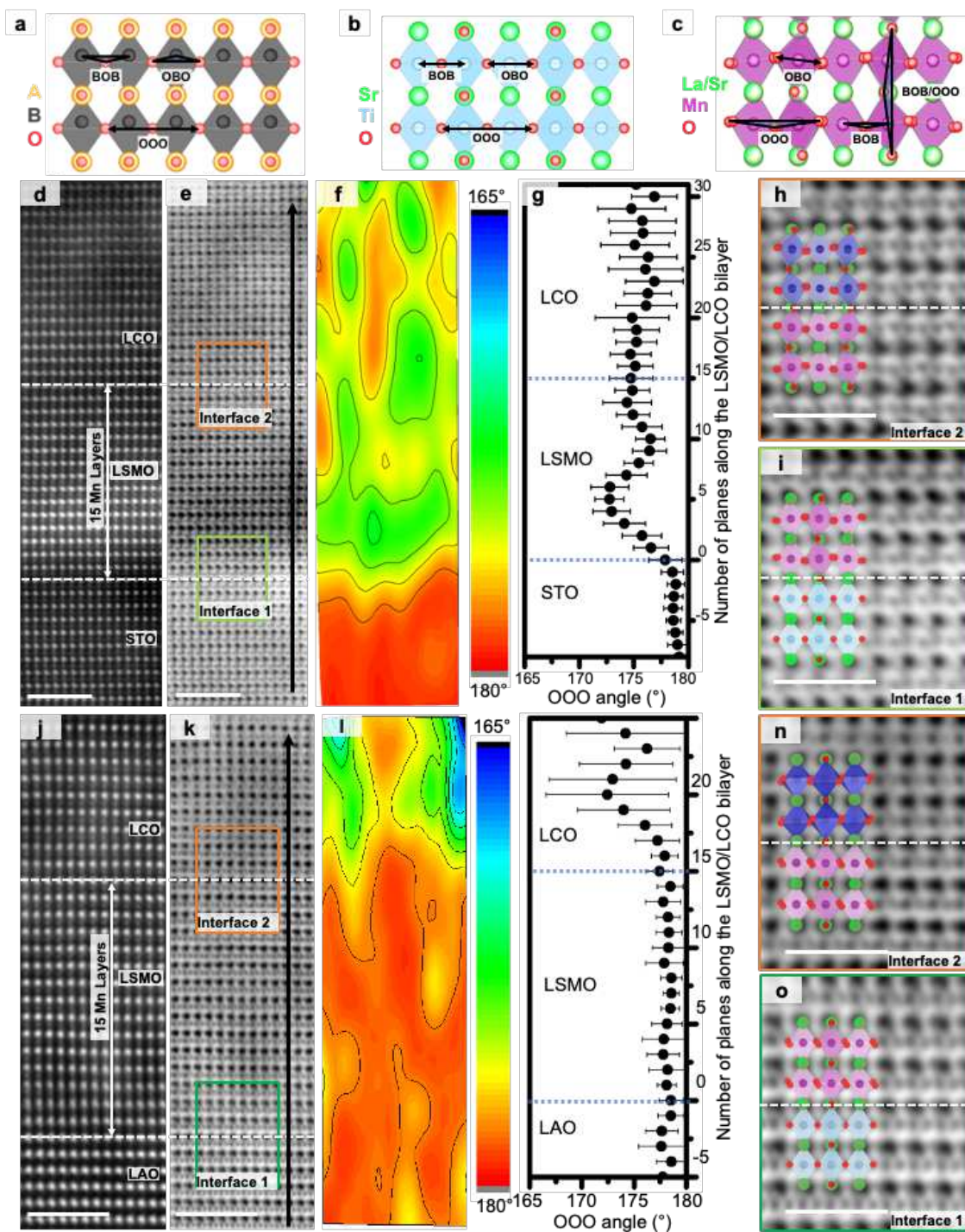
Figure 2| Octahedra tilt under strain of the LSMO/LCO BLs. a-c, Schematics depicting the selective detection of the octahedral tilt using the OOO_{proj} angles, whereas the BOB_{proj} does not effectively differentiate between octahedra tilt and distortion. **d-e,** HAADF-STEM (**d**) and ABF

micrographs (**e**) of the BL2 on STO substrate. **f,** The OOO_{proj} angles mapped as contours to the O coordinates and, **g,** the measured row-averaged OOO_{proj} angle with the standard deviation for each row plotted with respect to the planar distance of the BL2 on STO. A drastic change in the OOO_{proj} angle is observed at the LSMO/STO interface indicating octahedral tilting in the LSMO film, while a subtle change in the standard deviation of the OOO_{proj} angle is observed at the LCO/LSMO interface. **h-i,** Digitally magnified images of the two interface with the overlapped schematic structural model, depicting the absence of rotations in the TiO_6 octahedra of the STO substrate and the periodic checkerboard-like octahedral tilt in the MnO_6 octahedra of LSMO film and CoO_6 octahedra of the LCO layer. j-k, HAADF-STEM **(j)** and ABF micrographs **(k)** of the BL2 on LAO substrate. **l,** The OOO_{proj} angles mapped as contours to the O coordinates and, **m,** the measured row-averaged OOO_{proj} angle with the standard deviation for each row plotted with respect to the planar distance along the BL2 on LAO. The observed absence of the variation in the OOO_{proj} angles at the LSMO/LAO interface indicates that the octahedra tilting might be suppressed due to the compressive strain by the substrate, while the drastic variation at the LCO/LSMO interface might indicate that the effect of strain is reduced far from the substrate. **n-o,** Digitally magnified images of the two interface with the overlapped schematic structural models directly visualizing that the O atoms are coplanar along this projection. Scale bar in **(a, b, j, k)** represents 2 nm, and scale bar in **(e, f, n, o)** represents 1 nm. The projected TiO_6 and AlO_6 octahedra of the STO and LAO substrates are represented by the light blue octahedra, while the MnO_6 octahedra of LSMO and the CoO_6 octahedra of LCO are represented by the pink and dark blue octahedra, respectively in **(e, f, k, l)**.
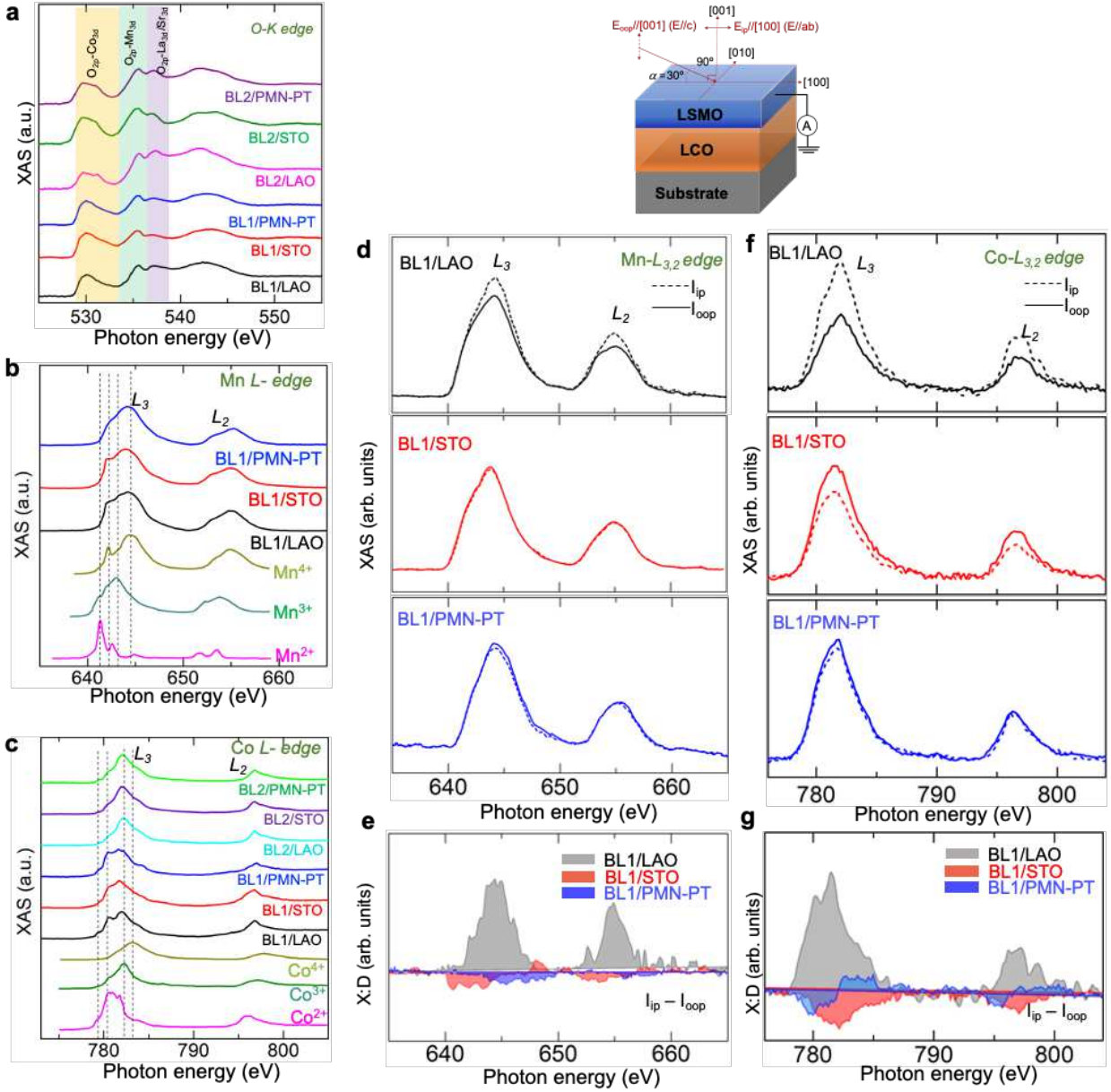
Figure. 3 | Strain mediated electronic structure and orbital polarization in the LSMO/LCO BLs. Elemental specific **a,** XAS at O *K*-edge for both sequence bilayers (BL1 and BL2). The colored area in XAS O *K*-edges represents the electronic hybridization between O $2p$ and Co $3d$ orbitals (transparent yellow); O $2p$ and Mn $3d$ orbitals (transparent green) and O $2p$ and La/Sr $3d$ orbitals (transparent purple). **b,** XAS measurement done on BL1 with Mn^{2+}, Mn^{3+}, and Mn^{4+} references at the Mn $L_{3,2}$-edges, the peak positions indicate that the BL1 are in mixed $Mn^{4+/3+}$ states. XAS data confirm the valence state of the Mn independent of the strain states for the BLs.

The spectra are vertically shifted for clarification. The details of Mn reference spectra are described in Supplementary Note I. **c,** XAS at the Co $L_{3,2}$-edge for BL1, BL2 show strong peaks at around 782.06 eV and 780.36 eV in consistent with the Co^{3+} and Co^{2+} ions respectively, which is independent of the strain states. The details of Co reference spectra are described in Supplementary Note I. **d-f,** XAS measured from linearly polarized x-ray parallel to the in-plane direction of the sample surface at the Mn $L_{3,2}$-edge (**d**) and Co $L_{3,2}$-edge (**f**) of the BL1 (measurement geometry at the top). **e,** The XLD was obtained from the difference for XAS measured with I_{ip} and I_{oop}, i.e. (I_{ip}-I_{oop}) for the BLs. The XLD spectra reveal higher out-of-plane orbital occupancy ($d_{3z^2-r^2}$ d_{zx}, and d_{yz} orbital) for the BL under compressive strain i.e. BL on LAO, while, in-plane orbital occupancy ($d_{x^2-y^2}$ and d_{xy} orbital) for the BL under tensile strain i.e. BL on STO and PMN-PT, indicating a clear anisotropic orbital occupancy induced in Mn $3d$ e_g orbitals (**e**) and in Co $L_{3,2}$-edge (**g**) by substrate induced strain. All spectra are collected at room temperature.
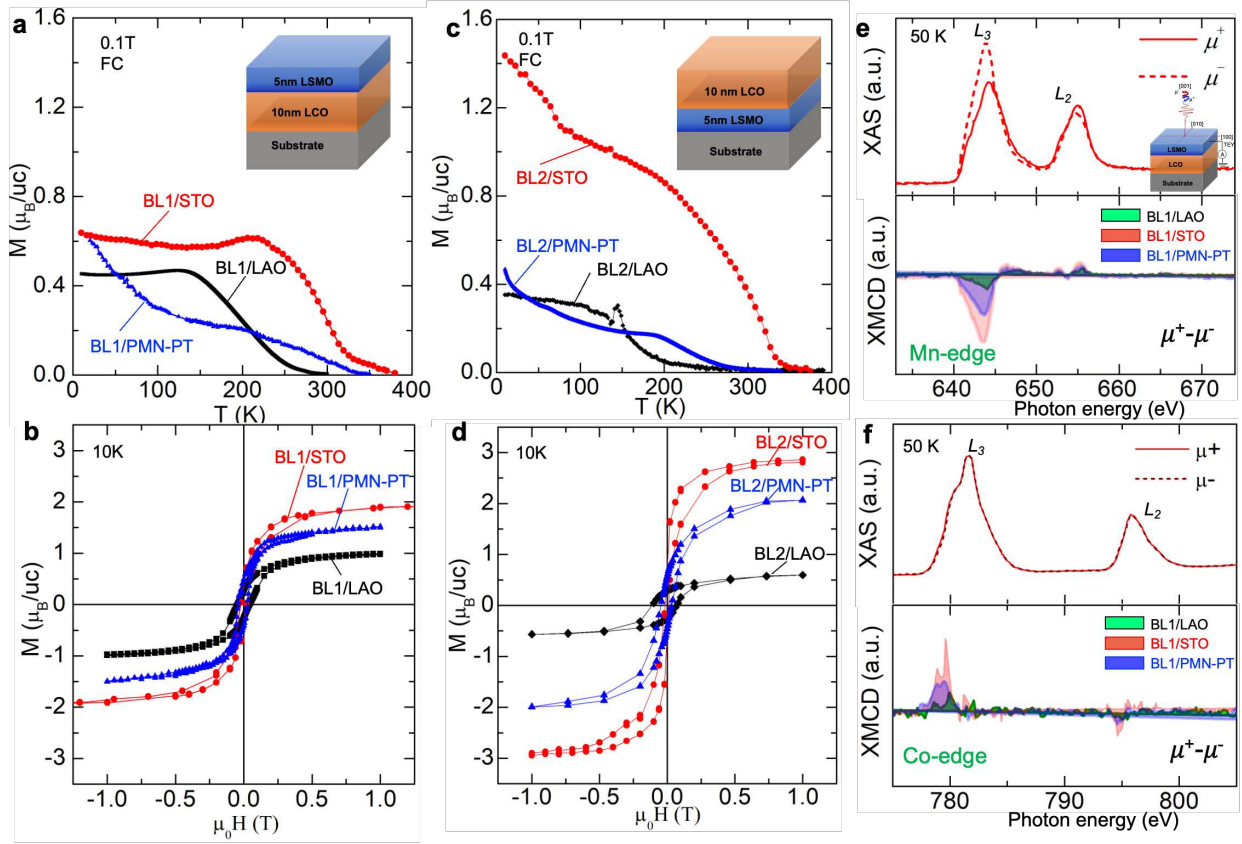
Figure 4| Magnetic properties of the BLs under strain. a, M-T measured at 0.1T after field cooled BL1 (BL1 on LAO, STO and PMN-PT). The data shows both LCO and LSMO layer in ferromagnetic nature for BL on STO and PMN-PT (under tensile strain) with an emergence of antiferromagnetic nature in BL on STO, while a suppressed ferromagnetism of LCO is revealed for BL on LAO. **b,** M-H loops of the BL1 are recorded at 10 K when a magnetic field is applied along the in-plane direction. BL1 on STO, PMN-PT shows higher saturation magnetization than on BL1 LAO. **c,** M-T measured at 0.1T after field cooled BL2 (BL2 on LAO, STO and PMN-PT). The data indicates the enhanced magnetization for BL on STO, keeping both LCO and LSMO ferromagnetism intact for the BL on STO and PMN-PT, while a spin reorientation around 150 K is seen for BL on LAO substrate. **d,** M-H loops of the BL2 recorded at 10 K when a magnetic field is applied along the in-plane direction. BL2 depicts similar behaviour like the BL1 including more enhanced saturation magnetization (with respect to BL1) on STO and PMN-PT. **e-f,** X-ray absorption spectra (XAS) (top panel) at Mn L-edges (**e**) and at Co L-edge (**f**) were collected at 50K

27

under 0.6T out of plane applied field for the BL1. The incident beam is normal to the film's surface. The calculated x-ray magnetic circular dichroism (XMCD) spectra (bottom panel of **e, f**) for the BL. Non-zero XMCD signal at the Mn *L*-edges and Co *L*-edges is clearly observed for the BLs. Thus, overall magnetization is less under compressive strain and higher in case of tensile strain irrespective of BLs. Opposite signs at the Co/Mn *L*-edge XMCD signals elaborates the unusual antiferromagnetic coupling at the Co/Mn heterointerface.
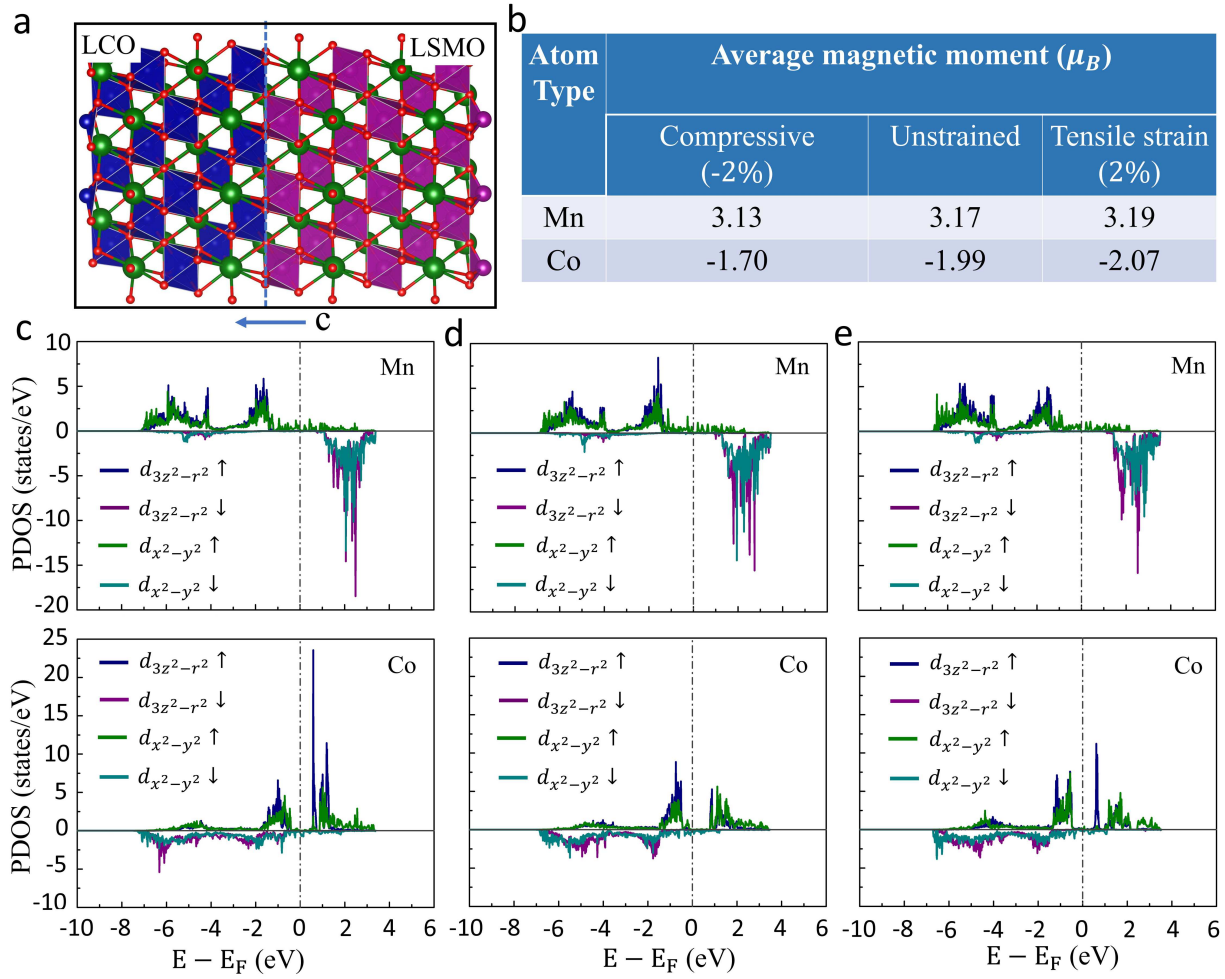
Figure 5| Strain induced orbital occupancies in BLs. a, The $3 \times 3 \times 1$ supercell LSMO/LCO bilayers considered for the first-principles calculations. Here, the crystallographic *c*-axis is indicated by a blue arrow. The tensile and compressive strains are applied along the other two crystallographic directions- *a*-axis and *b*-axis. **b,** The effect of tensile and compressive strain on the magnetic moment value of both Mn and Co is given in tabular form. It is clear that the magnetic moment of both Mn and Co atoms increases with tensile strain and decreases with compressive strain, respectively. The projected density of states for the orbital contributions for Mn (top panel) and Co (bottom panel) atoms of **c,** -2% compressive strained, **d,** unstrained, and **e,** +2% tensile strained BLs. The vertical dashed line at zero energy value indicates the Fermi level. The in-plane

d-orbital gets more occupied with tensile strain, while the occupancy of out-of-plane orbitals increases under compressive strain.

Supplementary Files

This is a list of supplementary files associated with this preprint. Click to download.

- ManuscriptLSMOLCOBLSupplementaryNP.pdf